Nuclear Engineering and Technology 56 (2024) 611–623

Contents lists available at ScienceDirect

Nuclear Engineering and Technology

journal homepage: www.elsevier.com/locate/net

Original Article

Analyses of International Standard Problem ISP-47 TOSQAN experiment with containmentFOAM

Myeong-Seon Chae [a,*], Stephan Kelm [b], Domenico Paladino [a]

[a] Paul Scherrer Institut (PSI), Forschungsstrasse 111, 5232, Villigen PSI, Switzerland
[b] Forschungszentrum Jülich GmbH, Jülich, 52425, Germany

ARTICLE INFO

Keywords:
TOSQAN
CFD
containmentFOAM
Hydrogen
Containment phenomena

ABSTRACT

The ISP-47 TOSQAN experiment was analyzed with containmentFOAM which is an open-source CFD code based on OpenFOAM. The containment phenomena taking place during the experiment are gas mixing, stratification and wall condensation in a mixture composed of steam and non-condensable gas. The k-ω SST turbulence model was adopted with buoyancy turbulence models. The wall condensation model used is based on the diffusion layer approach. We have simulated the full TOSQAN experiment which had a duration 20000 *s*. Sensitivity studies were conducted for the buoyancy turbulence models with SGDH and GGDH and there were not significant differences. All the main features of the experiments namely pressure history, temperature, velocity and gas species evolution were well predicted by containemntFOAM. The simulation results confirmed the formation of two large flow stream circulations and a mixing zone resulting by the combined effects of the condensation flow and natural convection flow. It was found that the natural convection in lower region of the vessel devotes to maintain two large circulations and to be varied the height of the mixing zone as result of sensitivity analysis of non-condensing wall temperature. The computational results obtained with the 2D mesh grid approach were comparable to the experimental results.

1. Introduction

In a nuclear power plant, the containment is the last barrier to prevent any release of radiative material to the environment. Therefore, containment integrity must be maintained in all the postulated Design Basis Accident (DBA), beyond DBA and severe accident (SA) [1] sequences.

The analyses of physical phenomena with safety relevance taking place in the containment of a nuclear power plant during postulated accidents are analyzed using a variety of advanced computational tools [2]. Due to the large-scale and geometrical complexity of a containment on one side, and the need for optimizing the computational costs on the other side, it would be necessary to evaluate various modeling approaches such as LP (Lumped Parameter) vs. CFD (Computational Fluid Dynamics), 2D (Two-dimension) vs. 3D (Three-dimension), coarser vs. finer meshes, etc. It is therefore important to assess, through code validation activities, the computational needs for analyzing experiments, performed in thermal-hydraulics facilities equipped with the instrumentation required to carry out the validation of the codes. The existing experimental database on LWR containment has been created over the last years operating facilities such as TOSQAN (IRSN, France) [3], MISTRA (CEA, France) [4], ThAI (Becker Technology, Germany) [5], ATLAS-CUBE (KAERI, Republic of Korea) [6], CIGMA (JAEA, Japan) [7], PANDA (PSI, Switzerland) [8,9], etc.

Phenomena associated with the hydrogen risk and in particular to hydrogen distribution in the containment during a postulated severe accident, include for example: convective flows produced by jets and plumes, diffusion, buoyancy forces induced by density differences, condensation occurring on relatively cold walls or initiated by activation of cooler or spray, sump re-evaporation, etc. [8].

Code benchmarks as ISP (International Standard Problems) [10], are carried out with blind (*i.e.* without knowing the experimental results) and open (by knowing the experimental results) phases to compare different codes and modeling approaches in their suitability to predict the phenomena evolution taking place during the experiments. The main objective of ISP-47 was to assess the capability of CFD and LP codes in the area of containment thermal-hydraulics and the experiments were carried out in TOSQAN, MISTRA and ThAI facilities [11,12].

Our focus in this paper is to analyze the TOSQAN experiments. The main outcomes of the ISP-47 TOSQAN benchmark with CFD and LP codes were published in the article [11]. In the analyses performed by

* Corresponding author.
E-mail addresses: myeong-seon.chae@psi.ch (M.-S. Chae), s.kelm@fz-juelich.de (S. Kelm), domenico.paladino@psi.ch (D. Paladino).

https://doi.org/10.1016/j.net.2023.10.038
Received 5 July 2023; Received in revised form 17 October 2023; Accepted 29 October 2023
Available online 5 November 2023

Nomenclature

CFL	Courant-Friedrichs-Lewy ($u\Delta t/\Delta l$)
D_m	Mass diffusivity [m/s^2]
d	Diameter of injection tube [m]
Fr	Dimensionless number, Froude number ($\rho_j u_j/(\rho_m - \rho_j)gd$)
g	Gravitational acceleration, 9.8 [m/s^2]
l	Length between mesh elements [m]
M	Molecular weight [mol/L]
Pr	Prandtl number (ν/α)
Sc	Schmidt number (ν/D_m)
T	Temperature [K]
t	Time [s]
u	Average fluid velocity in the direction of streamwise [m/s]
u_τ	Friction velocity ($(\tau_w/\rho)^{1/2}$) [m/s]
u'	Averaged axial fluctuating velocity [m/s]
V	Atomic diffusion volumes
v	Average fluid velocity in the direction of transverse [m/s]
v'	Averaged radial fluctuating velocity [m/s]
X_i	Molar fraction of species i
x	Distance from the wall (Transverse direction) [m]
y	Distance from the bottom (Streamwise) [m]
y^+	The dimensionless wall distance based on the low of the wall (yu_τ/ν)

Greek symbols

α	Thermal diffusivity [m/s^2]
β	Volume expansion coefficient [$1/K$]
δ	Kronecker delta
κ	von Karman constant
λ	Thermal conductivity [$W/m{\cdot}K$]
μ	Dynamic viscosity [$kg/m{\cdot}s$]
ν	Kinematic viscosity [m^2/s]
ρ	Density [kg/m^3]
τ	Shear stress [$kg/m\,s^2$]

Subscripts

cw	Condensing wall
eff	Effective
j	Injection tube
m	Mixture gases
ncw	Non-condensing wall
t	Turbulent
w	Wall

the benchmark participants [11] using CFD codes, the global thermal thermal-hydraulics phenomena including condensation taking place during the TOSQAN experiment were reproduced [11]. However, for the local analysis, the CFD simulation of the transient evolution show some discrepancies. Those discrepancies may be due to momentum and diffusion transport especially turbulent diffusivity under natural convection or weakly forced convection. Moreover, turbulence modeling seems to be the main reason for the discrepancies [11]. Meanwhile the analyses performed with LP codes did not lead to comparable predictions of gas mixture stratification during the evolution of the transient [11].

To gain more insights on the effect of facility wall temperature to the evolution of flow circulation pattern, Malet et al. [11] have investigated so called "virtual cases". One of the virtual cases identified as "V3" was defined with larger temperature difference between condensing and non-condensing walls with respect to original case of "steady-state 2" (Steam injection with jet configuration). With these analyses they identified inside the TOSQAN containment volume 4 distinct zones, *i.e.* recirculation, condensation region, injection region, natural convection. And they observed stopping flow position (mixing zone) in the middle of the vessel caused a free convective flow directed upwards together with the downward flow from the condensation process taking place in the facility wall. It was concluded that the large temperature difference caused stronger buoyancy along the hot wall.

Kelm et al. [13] analyzed the ISP-47 on containment thermal-hydraulics TOSQAN and ThAI experiments by using ANSYS CFX including gas thermal radiation model. As outcomes of these analyses, they highlighted the need for further model development for turbulence in buoyant and condensation flows. Moreover, they concluded that the mesh resolution is also a key issue as well as the model improvement.

As a general outcome of all the simulations for the ISP-47 TOSQAN can achieve a good agreement with measured pressure and velocity near the condensing wall [11,13,14].

In this article, we have analyzed the complete transient of the ISP-47 TOSQAN experiment which had a duration of about 20000 s with the CFD code containmentFOAM [15,16] which is as an open-source solver based on OpenFOAM. The containmentFOAM solver [15] is developed for the simulation of transport processes inside confined domains such as a nuclear reactor containment during postulated accident scenarios.

In the computational analyses, we conducted sensitivity studies for the buoyancy turbulence models with SGDH (Simple Gradient Diffusive Hypothesis) and GGDH (Generalized Gradient Diffusive Hypothesis). We have also carried out "virtual cases", considering non-condensing wall temperatures different than those in the actual TOSQAN experiment. Moreover, we provide a further specific phenomenological interpretation of the gas mixture flow pattern based on the results of our CFD analyses, which is formed, which is formed in each experimental phase due to the temperature differences between ambient and non-condensing wall. We conducted an analysis with a focus on the prominent models that are commonly regarded as the primary governing physical models to comprehend the TOSQAN experimental phenomena. It should be noted that physical models involving gas thermal radiation were not taken into account in this paper.

2. TOSQAN experiment for the ISP-47

2.1. TOSQAN facility

The TOSQAN facility was built at IRSN (France) to perform a variety of thermal-hydraulic studies related to nuclear safety (e.g. hydrogen risk and complex phenomena of heat and mass transfer, etc.). The TOSQAN experimental facility formed as the enclosed cylindrical vessel made of stainless steel. The size of TOSQAN facility is 1.5 m of inner diameter and 4.8 m of total height. In addition, total internal volume is 7 m^3. The injection tube which has a diameter of 0.0041 m is located in the lower and center of the vessel and the height of exit of injection tube is 2.1 m, the schematic view of the TOSQAN facility shows in Fig. 1. Detailed on description could be found in Malet et al. [11,12].

The TOSQAN facility is divided into 4 zones: an upper zone as a non-condensing wall (heated wall), a lower zone as a non-condensing wall (heated wall), a middle zone as a condensing wall (cooling wall) and a bottom zone as a sump region which is the same temperature with a non-condensing wall. The TOSQAN ISP-47 experiment investigates a multi-species gas mixture composed of air, steam and helium, where the latter simulates hydrogen gas behavior.

2.2. Initial and boundary conditions

The specific description of the initial and boundary conditions is given in Table 1. According to the initial condition, the total pressure is

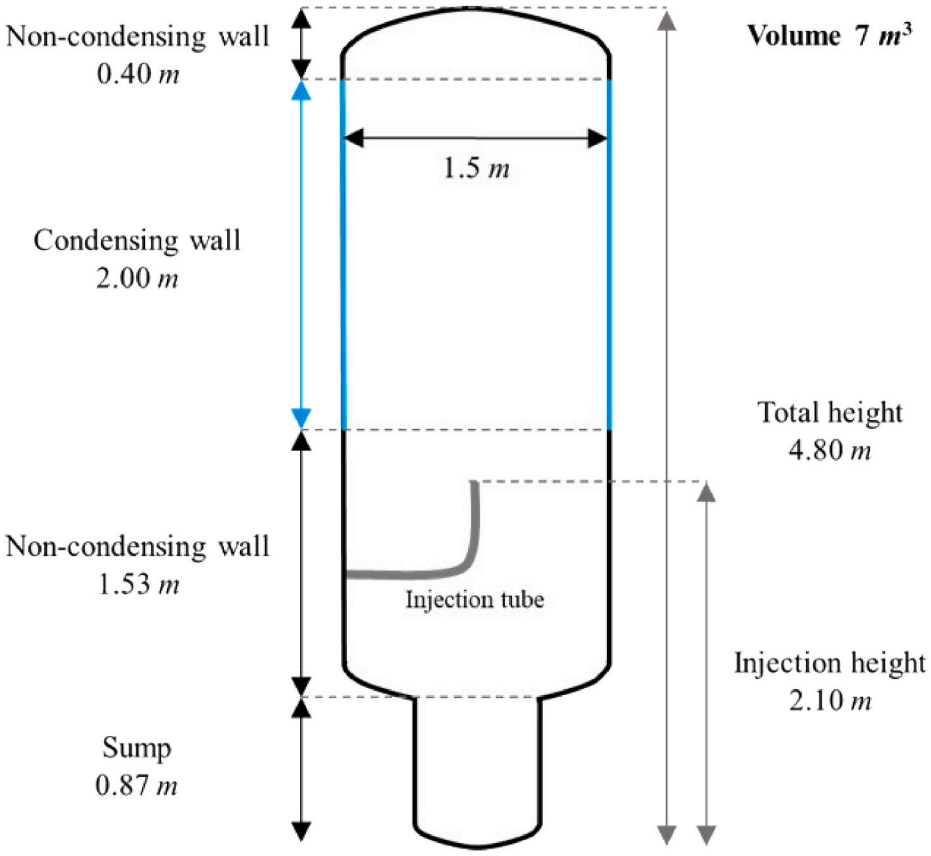

Fig. 1. The schematic view of the TOSQAN facility.

Table 1
Initial and boundary conditions.

Initial condition					
Total pressure					1 bar
Non-condensing wall temperature			Upper wall		122.0 °C
			Lower wall		123.5 °C
Condensing wall temperature					101.3 °C
Gas temperature					115.4 °C
Injected fluid temperature					124 °C
Volume fraction			Air		100 %
			Steam and helium		0 %
Boundary condition (as time sequences)					
Phase	Flow	Time sequences	Mean mass flow rate	Mean temperature	Froude number
A	Air injection	t_3 - t_4	3.16 g/s	125 °C	~8792
	Steady-state 1	t_4 – t_6	1.11 g/s	126 °C	~156
	Steady-state 2	t_6 - t_8	12.27 g/s	132 °C	~12718
	Steady-state 3	t_8 - t_{10}	1.11 g/s	126 °C	~156
	Air injection	t_{10} - t_{11}	3.16 g/s	126 °C	~8675
B	Helium injection	t_{13} - t_{14}	1.03 g/s	126 °C	~3637
	Steady-state 4	t_{14} - t_{15}	0.89 g/s	138 °C	~48

* The amount of 1.11 g/s for steam was injected all the time.

1 bar and temperature of non-condensing wall and condensing wall are about 122.0 °C and 101.3 °C respectively. At the initial condition, there is the only air without steam and helium with temperature of 115.4 °C. Injected fluid temperature set to 124 °C.

The boundary condition is shown not all the time sequences of the ISP-47 TOSQAN experiments but some sequences including four steady-states are addressed in Table 1 and Fig. 2. The specific condition can be given in Malet et al. [11,12]. There are two main phases of interest sequence to observe the mixing gas stratification and behavior in TOSQAN facility. First phase (Phase A) focused on two-gas-mixture, *i.e.* air and steam distribution for three specified steady-states over the two different pressure levels. Second phase (Phase B) concentrated on three-gas-mixture, *i.e.* air, steam and helium distribution for one specified steady-state. The dimensionless Froude number (*Fr*) is well known to be used to express for the relevant in fluid dynamic flow condition. It is a physical parameter that defined as relative force between inertia force ($\rho_j u_j^2$) and buoyancy force ($(\rho_m - \rho_j)gd_j$). When the *Fr* is more than 1 the flow is dominated by inertia force when vice-versa case the flow is dominated by buoyancy force. *Fr* of 1 means that the buoyancy force is comparable to inertia force. It can be expressed as:

$$Fr = \frac{\rho_j {u_j}^2}{(\rho_m - \rho_j)gd_j}. \quad (1)$$

Each phase of the experiment is characterized by various flow, namely, *i.e.* jet, plume and jet-plume conditions. The plateau region was just before the steady-state 1 and it is reached when there was balance between the wall condensation flow rate and the injection flow rate. The air injection state (t_3 - t_4) took place for the first seeding of TOSQAN vessel for the laser based velocity measurements. The steady-state 1 and steady-state 3 are characterized by steam-air jet-plume configurations. Also, steady-state 4 indicates the same flow condition, but for a three species mixture, *i.e.* air-steam-helium gases. The steady-state 2 is treated as a jet configuration with only steam.

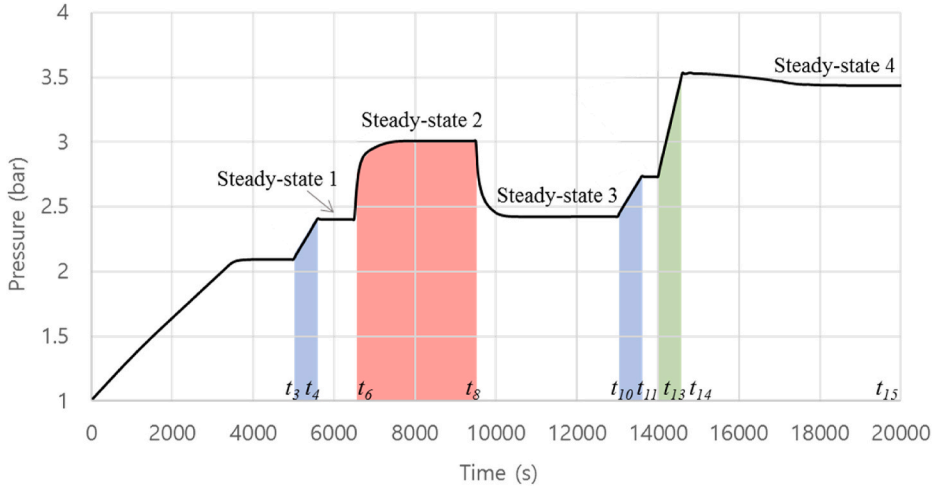

Fig. 2. General overview of the test sequences in ISP-47 TOSQAN experiments.

3. Modeling approach

In this study, the containmentFOAM CFD code [15] was used to analyze the experimental results of the OECD/NEA ISP-47 TOSQAN. The containmentFOAM package is a multi-physics toolbox based on OpenFOAM® (at the time of running the analysis version 6, currently version 9). It has been developed with the purpose of efficiently simulating transport processes inside confined domains for instance a nuclear reactor containment under postulated accident scenarios. FZJ (Forschungszentrum Jülich GmbH) leads the development activities of containmentFOAM [15]. The proposed baseline modeling approach for containment atmosphere mixing processes was adopted.

The containmentFOAM solver is based on the reactingFOAM solver for combustion with chemical reactions. It is a transient solver for compressible, turbulent flow with reacting, multiphase particle clouds and surface film modelling. However, it was considered the turbulent flow with buoyancy turbulence model and multi-species with the wall condensation modelling without combustion and chemical reactions in this case.

3.1. Governing equations

The unsteady Reynolds Averaged Navier Stokes (U-RANS) approach was selected for the analyses of TOSQAN experiments. This approach does not require a significantly resolved mesh and requires two additional transport equations for modeling turbulence [16]. The governing equations are shown in eqs. (2)–(5). The continuity eq. (2) can be solved together with N-1 species transport eq. (3). There is no chemical reaction among those of species and the total mass fraction (Y_k) of the N_{th} should be unity over the kind of species k. The diffusive mass flux ($\vec{J}_k$) is demonstrated by Fick's law. And $D_{k,eff}$ is the diffusion coefficient of the species.

$$\frac{\partial \rho}{\partial t} + \nabla \cdot \left(\rho \vec{U}\right) = 0 \tag{2}$$

$$\frac{\partial (\rho Y_k)}{\partial t} + \nabla \cdot \left(\rho \vec{U} Y_k\right) = -\nabla \cdot \vec{J}_k + S_{Y_k} \text{ where } \sum_{i=1}^{N} Y_k = 1 \text{ and} \tag{3}$$

Equation (4) shows the momentum equation and viscous stress tensor (τ) is defined as following. Where ν indicates the kinematic viscosity of the gas mixture and ν_t indicates the turbulent eddy viscosity. The δ is the Kronecker delta.

$$\frac{\partial \left(\rho \vec{U}\right)}{\partial t} + \nabla \cdot \left(\rho \vec{U} \otimes \vec{U}\right) = -\nabla p + \nabla \cdot \tau + \rho \vec{g} + \vec{S} \text{ where } \tau = \rho(\nu + \nu_t)\left[\nabla \vec{U} + \left(\nabla \vec{U}\right)^T - \frac{2}{3}\delta \nabla \cdot \vec{U}\right] \tag{4}$$

Total energy equation for the static enthalpy is shown in (5). The total enthalpy energy ($h_{tot} = h + K$) and $K = |U|^2/2$. The heat flux term could be transformed to eq. (6) according to $\lambda_{eff} = \lambda + \lambda_t$ and $\alpha_{eff} = \lambda_{eff}/(\rho c_p)$. More detailed explanation can be found in Ref. [15].

$$\frac{\partial (\rho h)}{\partial t} + \nabla \cdot \left(\rho \vec{U} h\right) + \frac{\partial (\rho K)}{\partial t} + \nabla \cdot \left(\rho \vec{U} K\right) = \frac{\partial p}{\partial t} - \nabla \cdot \vec{q} + \nabla \cdot \left(\vec{U} \cdot \tau\right) + \vec{U} \cdot (\rho \vec{g}) + \vec{U} \cdot \vec{S}_{mom} - \nabla \cdot \vec{q}_{rad} + S_h \tag{5}$$

where $\vec{q} = -\lambda_{eff} \nabla T + \sum_{k=1}^{N} \vec{J}_k h_k$.

and then $\vec{q} = \rho \alpha_{eff} \nabla h + \sum_{k=1}^{N} \rho(\alpha_{eff} - D_{k,eff}) h_k \nabla Y_k$. (6)

3.2. Physical models

Turbulence transport model k-ω SST in order to obtain turbulent eddy viscosity (μ_t) including buoyancy term is shown in eqns. (7) and (8). Where k is turbulent kinetic energy, P is turbulence production. Where ω is turbulence dissipation rate, μ and μ_t are fluid and turbulent dynamic viscosities, respectively, $P_{k,b}$ is turbulence production due to buoyancy, ν_t is turbulent kinematic viscosity (momentum eddy diffusivity). And β^*, σ_k, γ, β, σ_ω, $\sigma_{\omega 2}$, a_1, γ_1, C_3 denote modeling constants. And F_1, F_2 are blending functions with modeling constants. Where $P_{\omega,b}$ is turbulence dissipation due to buoyancy, τ is fluid shear stress tensor and S is the strain invariant. The modeling coefficients and blending functions are computed according to standard k-ω SST model. Where Pr_t and Sc_t have put 0.9. It means that turbulent thermal and mass eddy diffusivities are the same magnitude.

$$\frac{\partial (\rho k)}{\partial t} + \nabla \cdot \left(\rho \vec{U} k\right) = P - \beta^* \omega k + \nabla \cdot [(\mu + \sigma_k \mu_t) \nabla k] + P_{k,b} \text{ and} \tag{7}$$

$$\frac{\partial (\rho \omega)}{\partial t} + \nabla \cdot \left(\rho \vec{U} \omega\right) = \frac{\gamma}{\nu_t} P - \beta \rho \omega^2 + \nabla \cdot [(\mu + \sigma_\omega \mu_t) \nabla \omega] + 2(1 - F_1) \frac{\rho \sigma_{\omega 2}}{\omega} \nabla k \cdot \nabla \omega + P_{\omega,b} \tag{8}$$

$$\mu_t = \frac{\rho a_1 k}{max(a_1\omega, SF_2)},\ \text{where}\ \ P = min\left(\bar{\bar{\tau}}\nabla\vec{U}, 10\beta^*\omega k\right)\ \text{and}\ \ P_{\omega,b} = \frac{\rho}{\mu_t}\left[(\gamma_1+1)C_3 \cdot max\left(P_{k,b}, 0\right) - P_{k,b}\right]$$

We conducted the sensitivity study for the buoyancy turbulence models with SGDH (Simple Gradient Diffusive Hypothesis) [17] and GGDH (Generalized Gradient Diffusive Hypothesis) [18]. Turbulence production term ($P_{k,b}$) can be substituted as SGDH or GGDH buoyancy turbulence terms respectively, eq. (9) and eq. (10). In SGDH model, it accounts only for the density gradient in gravity direction.

$$\text{SGDH model}\ \ P_{k,b} = -\frac{\mu_t}{\sigma_t \rho}(g \cdot \nabla\rho) \tag{9}$$

On the other hand, GGDH model also considers cross-stream density gradients. Reynolds stresses are modelled using Boussinesq approximation as following as

$$\text{GGDH}\ \ \text{model}\ \ P_{k,b} = -\frac{3}{2}\frac{\mu_t}{\sigma_t \rho k}\left[g \cdot \left(\overline{u_j' u_k'} \cdot \nabla\rho\right)\right] \tag{10}$$

where $-\overline{u_j' u_k'} = \nu_t\left(\frac{\partial U_j}{\partial x_k} + \frac{\partial U_k}{\partial x_j}\right) - \frac{2}{3}k\delta_{jk}$.

Wilke's mixture model was selected in order to define mixture gas transport properties (φ_m) in containmentFOAM. Such transport propertiy of mixed fluid such as μ, λ can be calculated by Wilke's model [19].

Wall condensation is modelled by means of a diffusion-layer model, which allows computation of the local condensation rate based on cell values (control volumes adjacent to a condensing interface) and does not require the definition of bulk parameters like gas phase is the dominant transport resistance. Thus, the liquid condensate phase can be omitted. This implies that the boundary layer, including the viscous sublayer, is resolved ($y^+ \sim 1$) or modelled properly to account for all relevant effects, such as wall normal mass transfer and near-wall buoyancy. If more detailed explanation is needed it was given in Kumar et al. [20]. The condensation mass flux per unit area $\dot{m}''_{cond}$ can be described in eq. (12), where $Y_{H2O,w}$ is the steam mass fraction as the wall determining at saturation condition and $(\vec{J}_{H_2O,w} \cdot \vec{n}_w)$ means the wall normal diffusive flux of steam.

$$\dot{m}''_{cond} = \frac{1}{1 - Y_{H_2O,w}}\left(\vec{J}_{H_2O,w} \cdot \vec{n}_w\right) \tag{11}$$

In containmentFOAM, the condensation rate is implemented as a face-flux in the wall not by using source terms, which has shown to be less sensitive to the near wall mesh resolution.

At the wall, the Spalding profile is used for obtaining the turbulent viscosity, and the Kader wall function [21] has been implemented for both turbulent temperature and species diffusivities. In the viscous sublayer of the boundary layer the dimensionless mass fraction is defined as

$$Y^+_{i,lam} = y^+ \cdot Sc_i \tag{12}$$

Where Sc_i is the molecular Schmidt number of the species i. Within the turbulent sublayer of the boundary layer two formulations Kader is available, which account for the variation Sc_i in the boundary layer. Thus, the turbulent diffusivity in the near wall cell $D_{t,i}$ is dependent on the specie in a multi-component mixture.

$$Y^+_{i,turb} = \frac{Sc_{t,i}}{\lambda} \cdot \log(y^+) + \left(3.85 \cdot Sc^{1/3} - 1.3\right)^2 + \frac{Sc_{t,i}}{\lambda} \cdot \log(Sc) \tag{13}$$

Velocity scale is adopted as the value which is the blended with turbulent and viscous sublayers as follows

$$Y^+_{i,blended} = \left(Y^{+\ -4}_{i,lam} + Y^{+\ -4}_{i,turb}\right)^{-\frac{1}{4}} \tag{14}$$

To model multi-species gas diffusion, an effective binary diffusion model was adopted. The effective binary diffusivity of the species 'j' in the mixture $D_{j,eff}$ is calculated in eq. (15). And the Fuller model, eq. (16), was adopted to determine the pressure and temperature dependent binary diffusivity of the species j in species k [22].

$$D_{j,eff} = \frac{1 - X_j}{\sum_{i=1, i\neq k}^{N} X_k / D_{k,j}} \tag{15}$$

$$\text{where}\ \ D_{k,j} = \frac{0.00143T^{1.75}\left(\frac{1}{M_k} + \frac{1}{M_j}\right)^{\frac{1}{2}}}{p\left[\left(\sum V_k\right)^{\frac{1}{3}} + \left(\sum V_j\right)^{\frac{1}{3}}\right]^2} \tag{16}$$

3.3. Numerical settings

We used a two-dimensional (2D) domain with TOSQAN facility, and we have analyzed the entire ISP-47 TOSQAN experiment which had a duration of about 20000 s. It should be pointed out, that the previous computational analyses performed by the participants to the ISP-47 TOSQAN experiments, were focused on the steady-state conditions. Fig. 3 shows the mesh of the TOSQAN domain with side, front, and top views, which was generated using ICEM CFD and nodalization. This mesh grid could be treated as 2D model because this cell type was formed as a very thin 3D mesh with hexahedron, in other words, the wedge angle is 5°. For the mesh sensitivity studies, four different cases were made: (a) $y^+ \sim 15$ (9799 cells), (b) $y^+ \sim 9$ (10576 cells), (c) $y^+ \sim 1$ (13684 cells) and (d) $y^+ \sim 0.8$ (54736 cells) where y^+ is defined as the average value near the condensing wall. In order to find a suitable mesh grid. Specifically, (a), (b), (c) present the variation of y^+ near the boundary layer of the condensing wall and (d) is one of the finer meshes.

The smallest length of the cell size is approximately 0.03 m. As shown in Fig. 3, the higher resolution for the meshes are defined in the center region of the vessel, *i.e.* where is rising the injected fluid and near the wall were condensation take place (a) - (d). In the other regions of TOSQAN volume was used a coarser mesh. It should be pointed out that for the mesh used in these simulations are optimized according to the criteria of mesh quality, *i.e.* maximum skewness < 20, non-orthogonality < 65°, maximum aspect ratio < 60 [23]. For this case, it is confirmed that the max. skewness = 2.49625, the max. non-orthogonality = 14.2238 and the max. aspect ratio = 69.5647. The computation time was taken about 172800 s with four processors for the single case.

The containmentFOAM uses a segregated approach to solve the governing equations throughout the PIMPLE algorithm. In particular, the time step is chosen to maintain the mean CFL ≤ 1, while a local maximum CFL ≤ 10 is tolerated if PIMPLE convergence is satisfied [15]. All second order accurate schemes are employed. For the more details of the numerical methods, schemes and algorithm, the readers are referred to Kelm et al. [15].

Fig. 4 indicates the pressure distribution over time for each y^+value. Four cases are considered varying y^+; (a) $y^+ \sim 15$ (9799 cells), (b) $y^+ \sim 9$ (10576 cells), (c) $y^+ \sim 1$ (13684 cells) and (d) $y^+ \sim 0.8$ (54736 cells). The pressure evolution during the experiment is well captured in the simulation carried out using mesh (c). Thus, case of (c) can be treated as an achievable mesh convergence for the analysis of the TOSQAN experiments. Therefore, the analyses which are presented in this article are all obtained using mesh (c) $y^+ \sim 1$. In addition, the pressure prediction with the 2D mesh is comparable with the 3D analysis published in 2019 [13]. It should be pointed out the analyses with 3D meshes (Kelm et al. [15]) predicted circumferential motion and oscillatory separation of the boundary layer between the heated wall and cooled wall section, and these phenomena are not possible to be detected using a 2D mesh approach.

3.4. Sensitivity studies

Sensitivity studies were conducted to assess the effect of buoyancy on turbulence with k-ω turbulence model. The SGDH and GGDH models

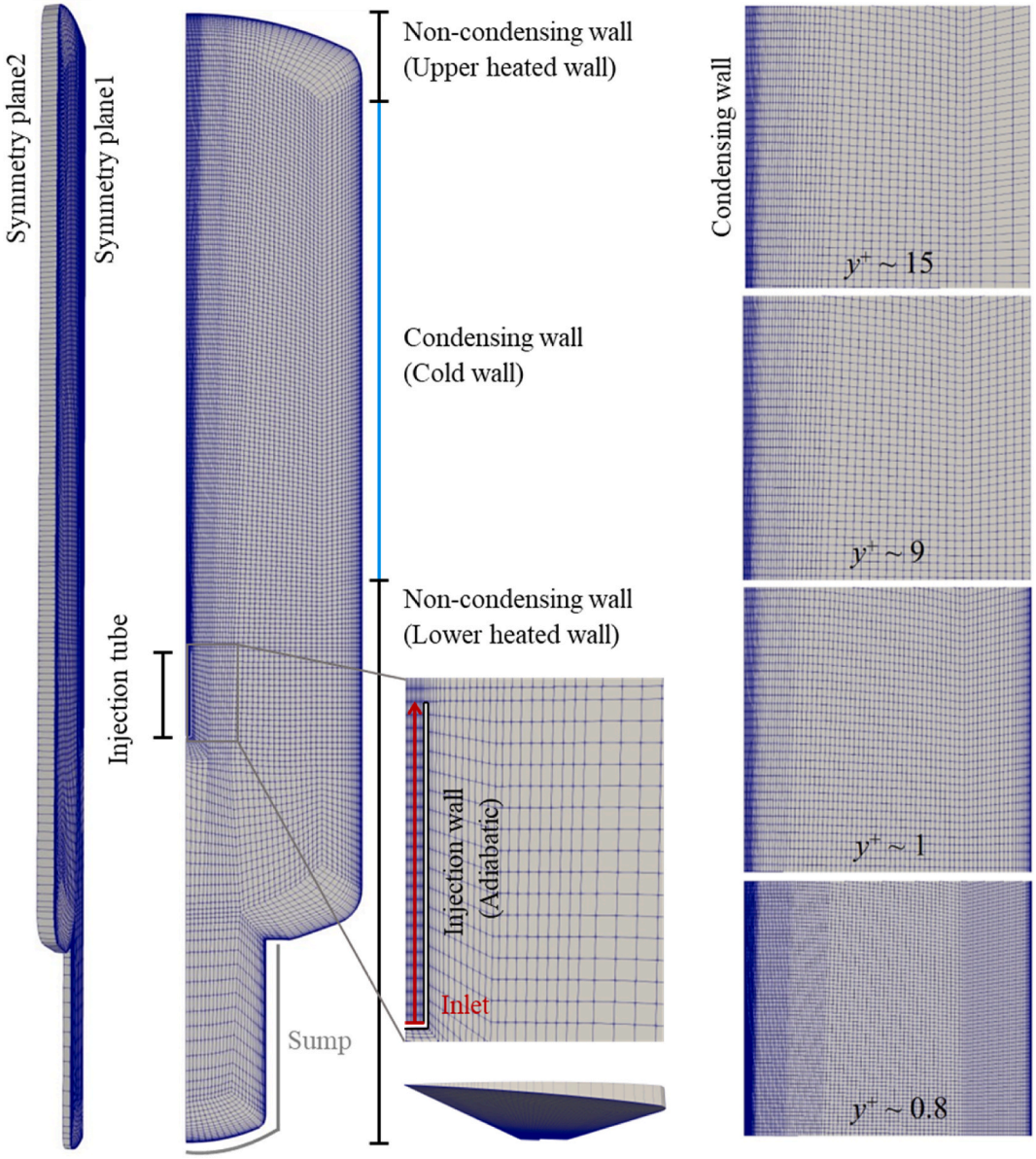

Fig. 3. Computational domain with mesh grid and nodalization scheme.

were used to confirm which model would be appropriate for turbulence production due to buoyancy forces in these TOSQAN experiments.

The temperature of the non-condensing wall was varied at 108 °C and 140 °C as the initial conditions with GGDH. It could be expected that there would be two dominant phenomena due to condensation and natural convection flows. Sensitivity study carried out to get insight of the dominated region by varying the non-condensing wall temperature within the feasible temperature range. Those temperatures are representative of containment temperature in some postulated accident scenario.

4. Computational results and discussion

The computational results and discussion include two main categories (sections 4.1 - 4.4): sensitivity analysis for the buoyancy-corrected turbulence models and (4.5) virtual cases considering the variation of the non-condensing wall temperature.

The first category of sensitivity analysis allows gaining insights on which models are more suitable for the analyses of these phenomena. The second category of sensitivity analysis aims to understand the effect of wall temperature on the evolution of containment flow pattern and gas mixture distribution.

The assessment of the computational results and phenomenological interpretation is carried out comparing variables such as: velocity, pressure, temperature, and gas mixture concentration. The discussion in this paper is focused on the turbulent flow model, the multi-species model, and the condensation model.

4.1. Reference case for the simulations

The computational results which are presented in this chapter are based on the finest boundary layer mesh (y^+~1) with 2-D model. Before discussing in details, the computational predictions of the experiments, it is needed to assess the impact of the two available models to consider production and dissipation of turbulence due to buoyancy forces, namely SGDH and GGDH. Moreover, to have a reference, we have run a case identified as None, where both SGDH and GGDH were switched off.

Fig. 5 shows that the pressure over the time for GGDH and SGDH are nearly identical and deviate slightly with that of the None in steady-state 4. This might be explained by the fact that the SGDH takes into account

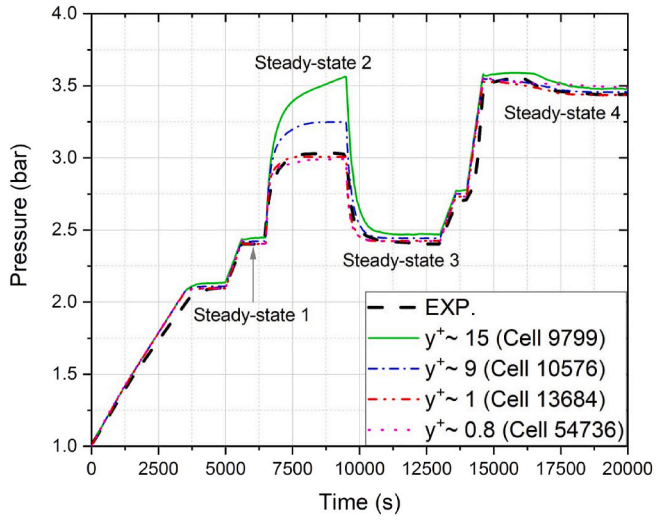

Fig. 4. Pressure distribution according to time such as the cell number.

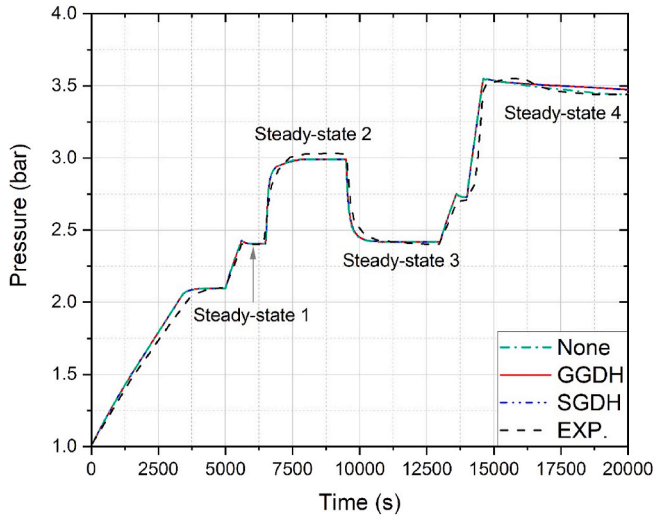

Fig. 5. Pressure distribution of the effect of buoyancy on turbulence model (None, GGDH, SGDH) according to time.

only for the density gradient in gravity and opposite-to-gravity direction. On the other hand, the GGDH also considers a transverse-stream density gradient. In the ISP-47 TOSQAN experiments, the main phenomenon is driven by the rising jet and condensation driven negative buoyant flow. Both models (SGDH and GGDH) produce similar results because the transverse-stream density gradient has no noticeable impact on the phenomenon taking place during the experiment. Nevertheless, in the following sections these aspects will be further assessed based on the predicted velocity profiles.

There was no significant discrepancy for the pressure over the time between experiments and calculation. The maximum relative difference is presented approximately 11 % at about 14000 s and it seems to be comparable results.

Afterward computational results are compared for steady-states 1, 2 and 4 since the flow conditions of the steady-state 1 and 3 are characterized by a jet-plume configuration with two-species. The measurement positions were fixed at five locations such as vertical axis with a center of the vessel and a half of the radius of the vessel and horizontal axis with 2.1 *m*, 2.8 *m* and 4.0 *m* from the bottom of the vessel.

4.2. Analysis of velocity distribution

4.2.1. Assessment of predicted flow velocity over the elevation

Fig. 6 indicates the velocity of the gas mixture in the upward direction according to the elevation of center of the vessel for experiments and calculations. Fig. 6 (a) corresponds to those of the steady-state 2 which is the jet configuration and Fig. 6 (b) corresponds to those of the steady-state 1 and 4 as the jet-plume configurations. The velocities were compared with None, SGDH and GGDH.

As shown in Fig. 6 (a) all of the results whether are experimental results or calculations present the maximum velocity near the exit of the injection tube. The velocity gradually decreases as increasing the elevation of the vessel. It was found that the calculated velocities represent well the experimental results. This is due to the fact that this flow condition corresponds to the jet configuration which is dominated by forced convection not buoyancy forces. In other words, typically, the turbulence model is given for jet configuration with dominated forced convection, and not combined jet and plume configuration or plume configuration despite the buoyancy term is included in turbulence model.

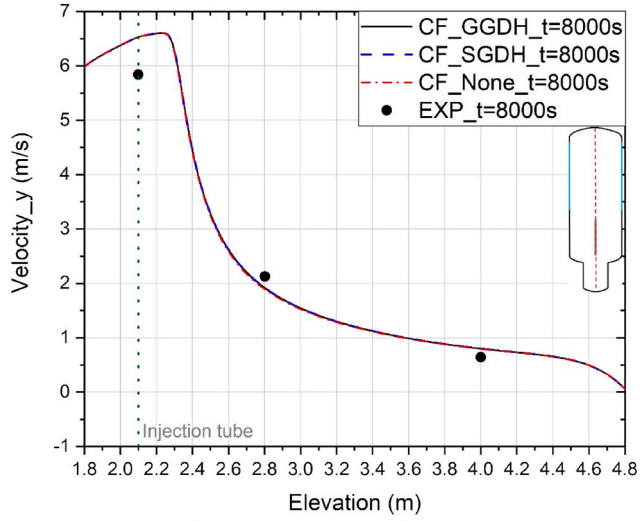

(a) Steady-state 2 (t=8000 s)

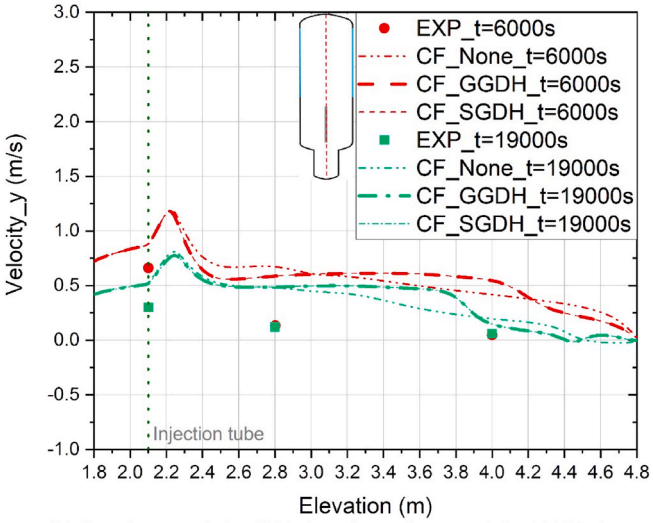

(b) Steady-state 1 (t=6000 s) and steady-state 4 (t=19000 s)

Fig. 6. Comparison of velocities between experiments and calculations (GGDH, SGDH) over time.

In Fig. 6 (b) shows that the velocities gradually decrease over the elevation. However, the calculated velocities have different behavior compared to the experiment. The velocity distribution has a peak near the exit of the injection tube and has a constant value and gradually decreases over the elevation. The reason why there exist the peak velocity is due to the fact that the buoyancy plume is added to the jet flow enhancing flow acceleration and dispersion.

It should be pointed out that the larger discrepancy between the computed velocity and the measured velocity in the experiment, over the elevation *i.e.* in Fig. 6 (b) corresponds to the jet and plume flow conditions. The reason for those larger discrepancies is explained by the fact that the steady-state 1 and 4 are not 'jet configuration' flow but combined 'jet and plume configurations'. The Froude numbers ($Fr \sim 48$, $Fr \sim 156$) indicate that the flows in steady-states 1 and 4 are driven by buoyancy forces.

Generally, the calculations for all of the steady states tended to a bit over-predict the experimental results. This discrepancy may be attributed to the impact of pipe bending, resulting in three-dimensional flow and potentially leading to an inhomogeneous flow with swirl. This constraint could be one of the limiting factors when simulating three-dimensional flow.

It is found that the velocities calculated according to elevation in all steady-states, shows no differences between the SGDH and GGDH models. Even if the cross-stream density variation was considered in the GGDH unlike in the SGDH, the velocity has not different since the primary flow in this phenomenon was the vertical-thermal plume with jet flow. The main difference is observed for the None case, in the upper part of the vessel, e.g. from 3.2 *m* to 4.2 *m,* where forced convection is not the main flow regime.

4.2.2. *Assessment of predicted flow velocity over the transverse direction*

Fig. 7 shows the comparison of velocity vector between experiments and calculations. All of the experimental velocity in Fig. 7 are mean velocity measured by LDV (Laser Doppler Velocimetry). Fig. 7 (a) shows the velocity according to the radial position at three heights in steady-state 4. Fig. 6 (b) shows the velocity at a fixed height of the vessel for each steady-state 1, 2 and 4.

The velocity shows the maximum value in the center of the vessel for both experiments and calculations in Fig. Fig. 7 (a) and (b). In particular, the velocity near the exit of the injection tube in Fig. 7 (a) and steady-state 2 (Jet configuration) in Fig. 7 (b) have higher velocities than other conditions. While the calculated velocities over the radial positions show some deviation with the experimental values in the center of the vessel, the velocities at other positions appear to be similar. The reason of the differences could be a limitation of the 2D modeling approach when applied to buoyant plume for which a 3D approach would be more appropriate. Overall, the calculated velocity magnitudes are in good agreement with the experimental results except for those in the middle of the vessel (Fig. 7 (a), (b)).

Fig. 8 compares the wall normal velocity profile between experiments and calculations according to radial position at steady-state 2 ($t = 8000\ s$) near the condensing wall at 2.8 *m* of height of the vessel.

The velocities in the experiments are measured by PIV (Particle Image Velocimetry) near the condensing wall is close to 0. The downward flow velocity steeply increases until $-0.725\ m$ of radial position. Moreover, the velocity gradually decreases according to the radial position. From Fig. 8 can be deduced that there is a resulting flow forming by the combination of "condensation" and "residual" flows. Due to the residual flow originated downward, the peak velocity is measured at about $-0.725\ m$.

In the calculations, the profile of the flow velocity is qualitatively similar to that of the experimental results. However, the maximum velocity is located very close to the condensing wall, in contrast to the experimental results. The velocities are not always well reproduced by the CFD calculations with the 2D approach due to the presence of thermal and dynamic boundary layers forming in the condensing wall.

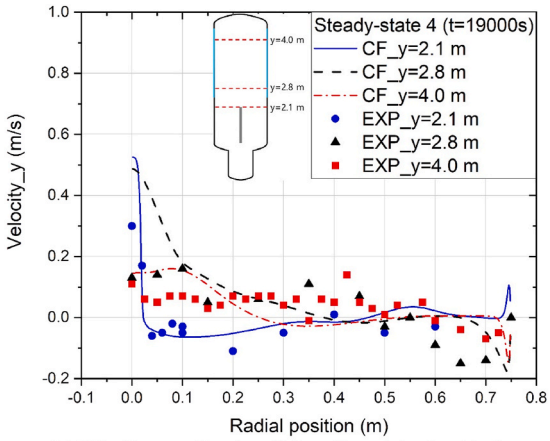

(a) Velocity according to radial position at steady-state 4

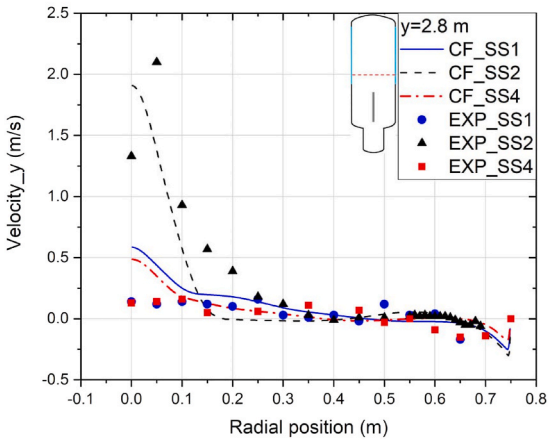

(b) Velocity according to radial position at height 2.8 *m* in steady-state 1, 2 and 4

Fig. 7. Velocity validation between experiments and calculations.

Moreover, it should be considered that film condensation is not expected to occur uniformly in the whole condensing wall. Therefore, the comparison between computational and experimental results near the wall provide an overall qualitative trend for the flow velocities.

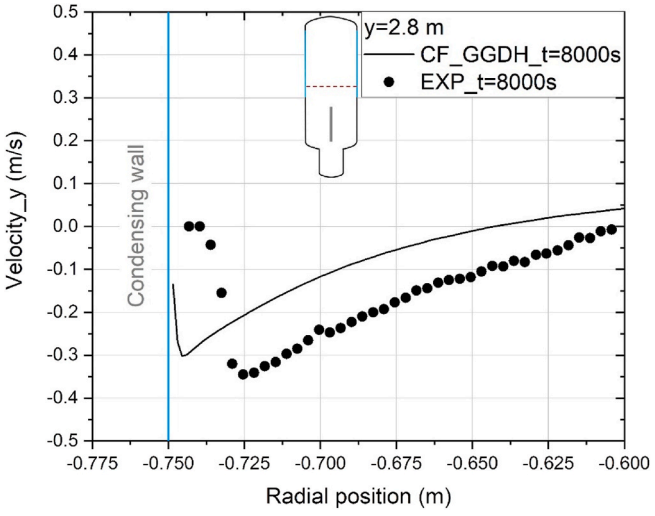

Fig. 8. Velocity distribution according to radial position at steady-state 2 on the condensing wall.

4.3. Analysis of gas mixture temperature distribution

The gas temperature distribution according to the elevation of the vessel height (Fig. 9), has similar tendency to that of velocity (as shown in Fig. 7). It was observed that the temperatures in the injection tube which represent the injection temperature boundary conditions is apparently the same in both experiments and calculations (GGDH) in all the steady-state 1 and 2 (6000 *s*, 8000 *s*). It should be noted that then, the temperature decreases with the increasing of vessel elevation and the calculation results predicted reasonably well the experimental results. In the calculations, the knee point for the temperature distribution is located at about 2.2 *m* elevation. This is due to the fact that the injecting fluid is continued until a certain elevation belonging to the potential core and then the fluid is dispersed. These knee points have different elevations between 6000 *s* and 8000 *s* due to the different mass flow rates.

Fig. 10 shows the temperature profile at 2.675 *m* of elevation from the bottom of the vessel near the condensing wall. The remarkable difference between experiments and calculations is that the calculated temperature is lower than that of experimental results very near to the condensing wall. The reason for these differences could be due to the thickness of boundary layer in the mesh grid. Because the first cell distance from the condensing wall is about 0.001 *m*. While the thickness of film condensing flow is known as 0.05–0.2 mm in the experimental results [24]. With the exception of the temperature measured very near the condensing vessel the computational results are in very good agreement with the experimental results.

4.4. Analysis of steam and helium volume fraction at steady-states

Fig. 11 shows the comparison between computational and experimental results for steam and helium volume fractions Fig. 11 (a) shows the steam volume fraction according to elevation at steady-state. The calculation results are in good agreement with the experimental results and the maximum relative difference is about 5 %. For both experiments and calculations, the steam volume fractions below and above the injection tube are similar. In the calculation results the steam volume fractions in the upper region of the vessel are higher of about 9 % than those of lower region of the vessel, due to condensation of steam from the mixture. It means that the steam is highly mixed with air and uniformly spread regardless of lower and upper part of the vessel because it is injected with high mass flow rate during steady-state 2.

Fig. 11 (b) provides steam and helium volume fraction at steady-state 4 characterized by a multi-species flow with steam, helium and air. The

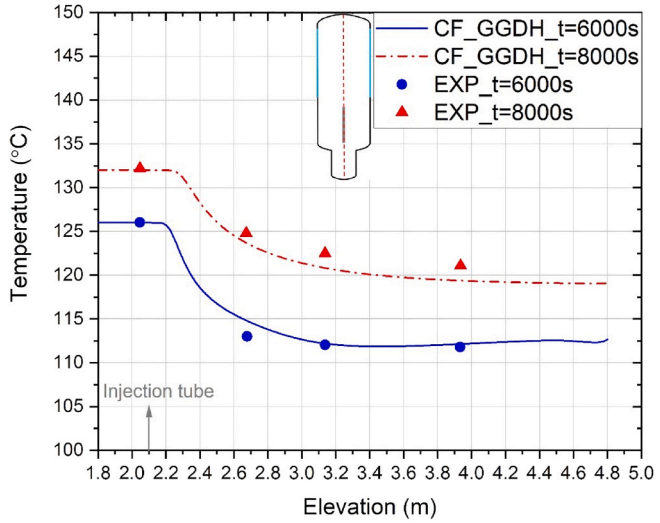

Fig. 9. Temperature distribution according to center of elevation.

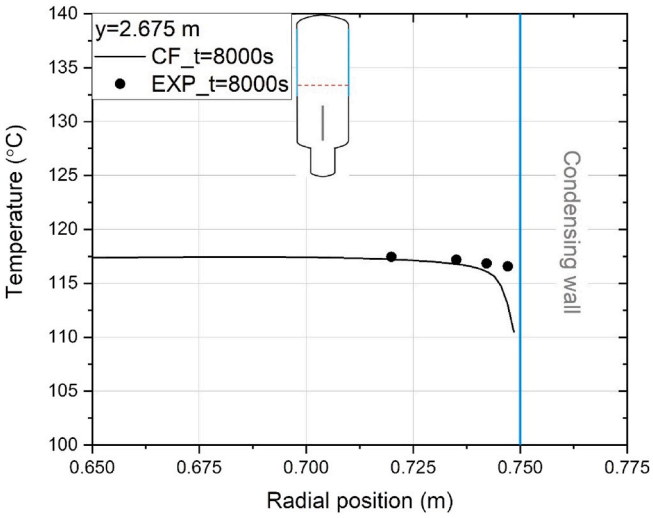

Fig. 10. Temperature distribution according to radial position (Condensing wall).

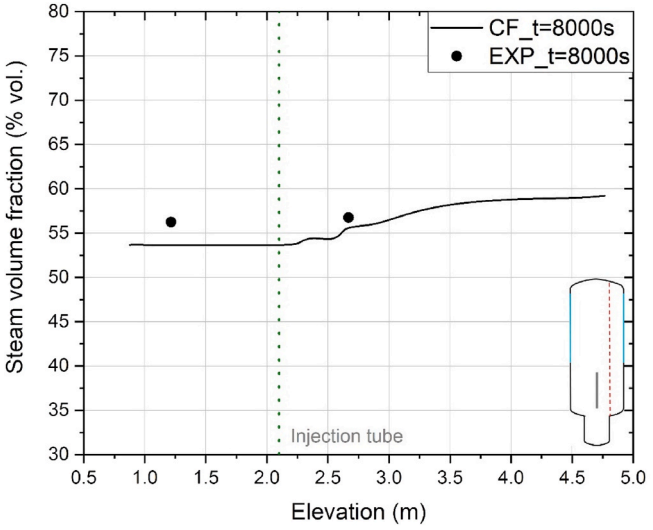

(a) Steam volume fraction (Steady-state 2)

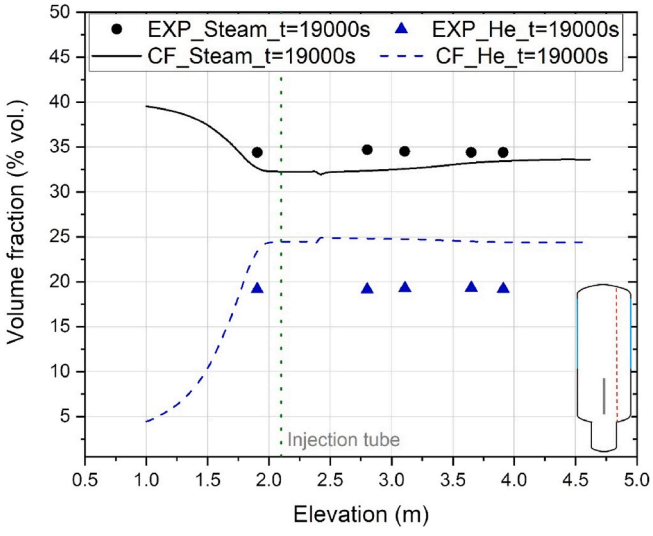

Fig. 11. Steam and helium volume fraction according to elevation of the half in vessel.

maximum relative differences between calculation and experimental results of volume fraction in steam and helium are about 7 % and 25 %, respectively. The calculated steam volume fraction gradually decreases with the increasing of elevation below the injection tube exit elevation (approximately from 40 % to 32 %) and it has almost 32 % volume fraction above the injection tube exit elevation. On the other hand, in case of helium volume fraction it steeply increases below the injection tube exit elevation and it has almost 25 % volume fraction in above the injection tube. This can be explained by the fact that helium which is lighter than steam was injected and accumulated in the upper region of the vessel.

It should be noted out that in the experiment the helium concentration is about 20 % in the vessel above the helium injection. It can be figured out that also in previous studies [24], related to the ISP-47, the helium concentration calculated by many of CFD and LP codes was over-predicted by a minimum 25 % and a maximum 75 % deviation which could be due to turbulence model and buoyancy flow. As follow-up study, containmentFOAM could be validated with other experiments (e.g. PANDA SETH Test 25 [25,26]), performed with three gases which have phenomena compared with the TOSQAN ISP-47.

4.5. Sensitivity study for variation of heated wall temperature

Fig. 12 indicates the streamline for averaging velocity in the flow field. Fig. 12 (a) shows a representative streamline with steady-state 1. Fig. 12 (b) shows the velocity streamlines according to flow conditions for steady-state 1, 2, 4. The magnitude of the velocity does not show a relative velocity of each temperature condition but the absolute velocity in its field. All the results were obtained with the GGDH model which is the buoyancy-corrected turbulence model.

It could be observed that there are two large circulation streams in the upper and the lower region of the vessel as shown in Fig. 12 (a). In the upper region of the vessel, the circulation consists of jet-plume flow, residual flow, stagnant flow and entrained flow. The jet-plume flow can be defined as oriented flow configuration whether jet or jet and plume. The residual flow is along with top plane of the vessel due to physically blocked. Besides, the stagnant flow is formed as a small circulation in the corner with top of the vessel. One of the major flow components in the upper region of the vessel could be the entrained flow combined with condensation flow and the residual flow.

In the lower region of the vessel, the flow is dominated by natural convection induced by the temperature difference between the ambient and the heated wall.

The mixing zone, located between the upper and lower circulation flows, is formed by the resulting flow with entrained and natural convection flows. It means that the region is characterized by the exchange of heat and momentum between the upper and lower regions. For this reason, the height of the mixing zone boundary is expected to depend on the magnitude of the velocity of two circulation stream.

As shown in Fig. 12 (b), it should be noted that the height of the boundary region noticeably decreased in steady-state 2 compared to that of the steady-state 1 and 4.

For the steady-state 2, the upper circulation has the high mass flow rate of steam which corresponding to the jet configuration. In this case the stagnant flow occurs in the corner at the lower region unlike with steady-state 1 (In this case, the stagnant flow is located on the corner in the upper region of the vessel).

For the steady-state 4, the flow behavior seems to have a chaotic pattern in the lower region of the vessel. The overall flow pattern is characterized by scattering small circulation stream. This flow pattern is caused by low mass flow rate and overall distribution of the mixture densities. Thus, steady-state 4 can be treated as quiescent state except for the area near the condensing wall and the mixing zone area.

Fig. 13 illustrates three cases of streamlines with varying non-condensing wall temperature. It shows the effect of the heated wall temperature from the mixing zone variation for in steady-state 1, 2 and 4, *i.e.* (a) 120 °C, (b) 140 °C, (c) 108 °C. The streamline and the average magnitude velocity over the non-condensing wall temperature on half of the vessel are placed on the left and right side of the figure respectively.

In steady-state 1 (SS1), both cases of streamline (a) and (b) have a similar flow pattern like as two large circulations in the upper and the lower region of the vessel. As shown in the average velocity magnitude, the tendency for both (a) and (b) is quite similar, showing the peak velocity according to the elevation. The main difference between (a) and (b) is the shape of the circulation in the upper region. Due to the high buoyant flow caused by the upper non-condensing wall in case of (b), the shape of the upper circulation does not seem to be nonintact compared to the (a). On the other hand, as shown in (c), there is no large circulation stream not only in the upper but also in the lower region. This is because the driving force is too low to make a large circulation induced by the temperature difference between the non-condensing wall and the ambient.

In steady-state 2 (SS2), case (a) shows the two circulations in both regions including stagnant flow in the lower region of the vessel. Whereas case (b) has the distorted circulation in the upper region of the vessel. In case (c), there is no circulation pattern in the lower part of the vessel. The most of remarkable thing is that the downward near the wall entrained flow has invaded into non-condensing wall. According to the magnitude of velocity, the average magnitude velocity of the (b) in the lower region of the vessel was observed a quite large velocity more than those of (a) due to large buoyancy. In addition, the location of the boundary with the mixing zone that indicates the second velocity peak with (b) has been shifted slightly towards to the upper region of the vessel more than in the original case (a). This is due to the fact that the high buoyancy force is induced by the large temperature difference between the wall and the ambient in the lower region of the vessel. Meanwhile, when comparing between (a) and (b) in the top region of the vessel, case (a) shows a rather high magnitude of velocity (~0.4 m/s). This can be explained that because case (a) is dominated by jet and condensation flows, whereas case (b) has a significant buoyant flow in the upper non-condensing wall (the height of the heated wall of 4.4 *m* from bottom of the vessel) of the vessel of it. It can be shown that due to the buoyant flow which has a different orientation with the jet and condensation flows, the resulting total velocity resulted reduced in the upper region of the vessel.

In steady-state 4 (SS4), it is noticeable that the streamline of case (a) is similar to that of the case (c) in steady-state 1. This means that the effect of the natural convection revealed by the small temperature difference between the wall and the ambient would be similar to the effect of the three-gas species. On the other hand, in case (b) it can be observed that two circulations remain in the lower and upper regions of the vessel owing to the intensive high buoyancy flow. The case (c) can be considered as a quiescent state as far as the velocity is concerned.

Stagnant flows were observed in both case (a) and (b). The stagnant flow can be formed in the region of low velocity either in the relatively whether upper or lower region of the vessel. For the case (a) of steady-state 1 and case (b) of steady-state 4, the stagnant flow occurred in the upper region where has low velocity relative to the lower region of the vessel. The case (a) of steady-state 2, the stagnant flow has in the lower region of the vessel as the same reason. The comparison of the steady-state 1 and 2 describes that the stagnant flow could be form in place where has very low velocity and this can happen in the upper or lower region of the vessel depending by the overall test boundary conditions.

5. Summary and conclusions

The containment phenomena taking place in the ISP-47 TOSQAN experiment were analyzed with the CFD open-source solver containmentFOAM which is based on OpenFOAM. For the analyses, several physical models were taken account.

With respect to the k-ω SST model, the sensitivity study was conducted for the SGDH and GGDH models which are the buoyancy-

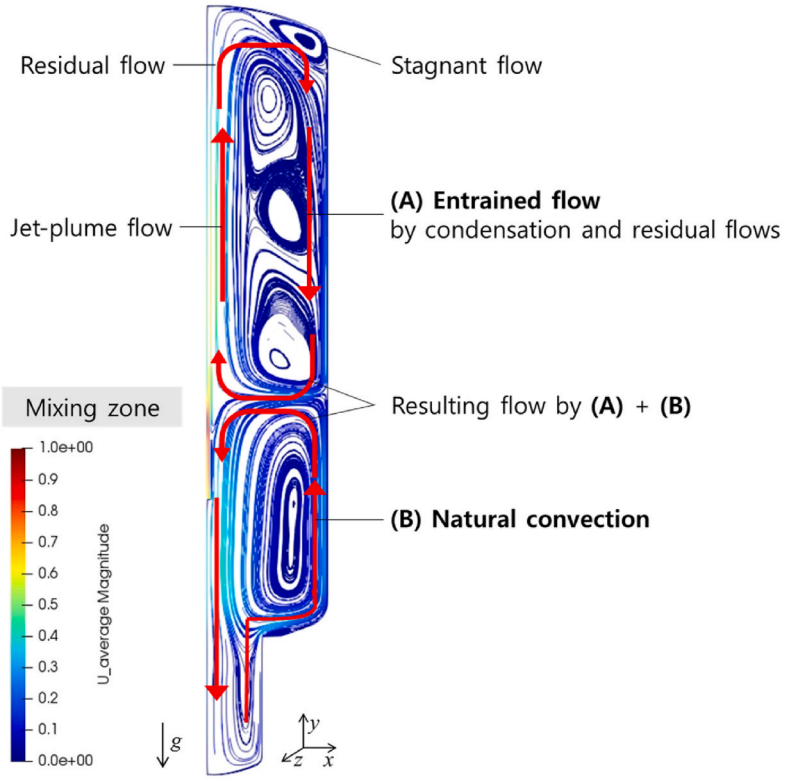

(a) Representative streamline (Steady-state 1)

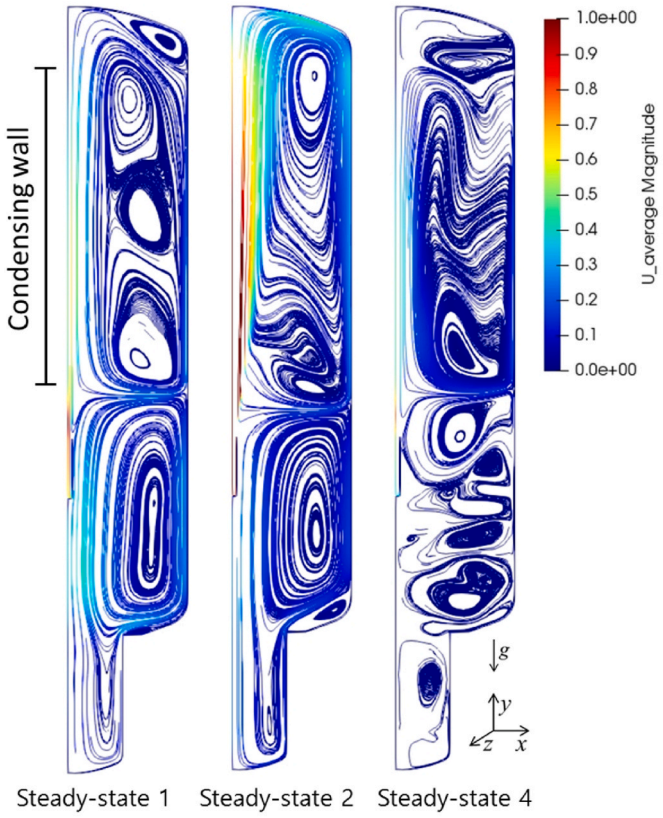

(b) Streamline according to steady-states

Fig. 12. Streamline in all steady-states.

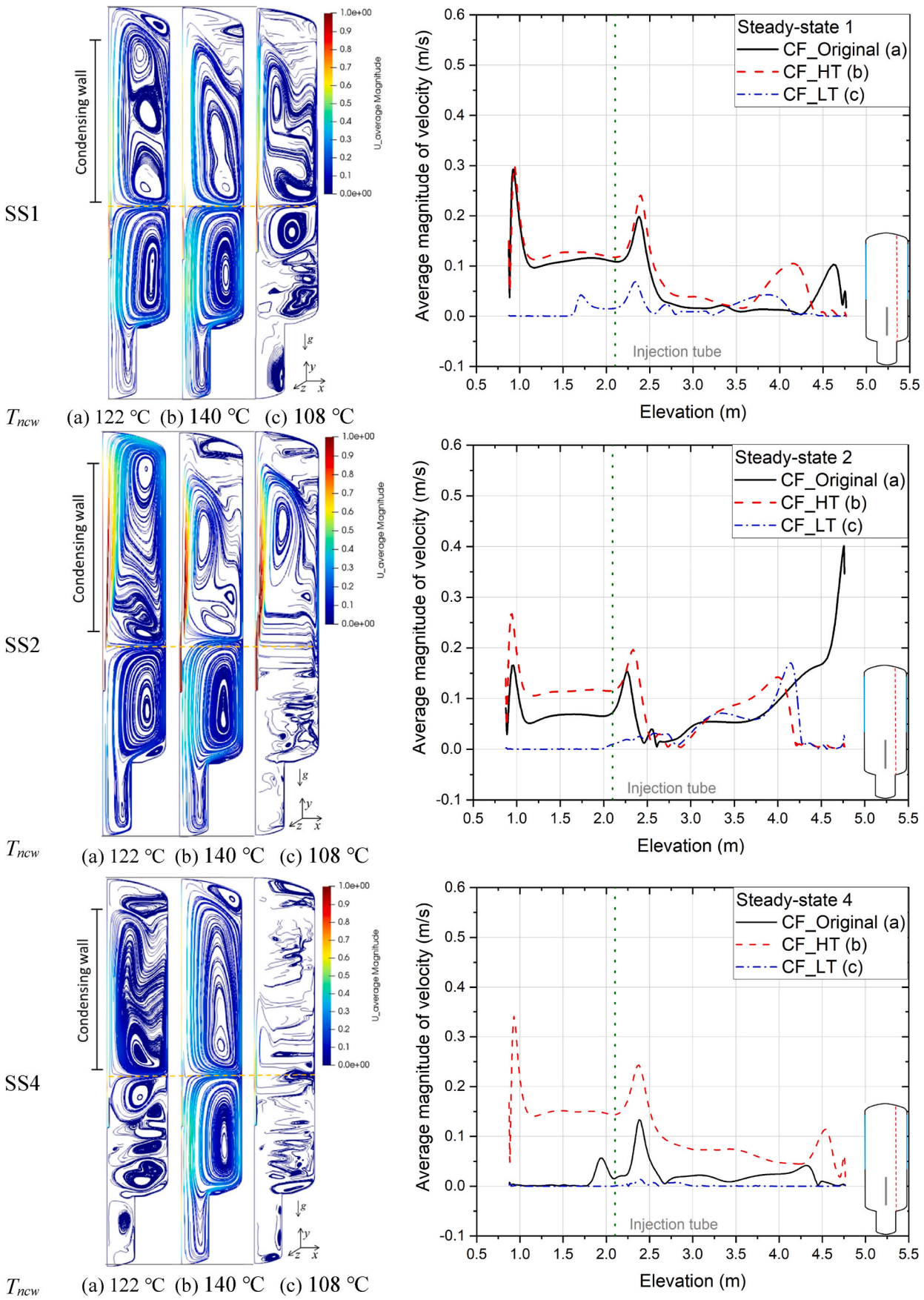

Fig. 13. Streamline according to the wall temperature.

corrected turbulence source terms. The flow condition was characterized by two main flow configurations, namely jet, combined with jet and plume. To define the transport properties of the mixture gases, Wilke's mixture model was adopted for these analyses. The condensation face-flux model was applied, and Kader model was used to calculate the condensation rate. The Fuller model was used to determine the mass diffusivity coefficient.

First, the outcomes of these analyses shows that the case with the y^+ ~1 (the number of cells 13684) calculates well the experimental results. The results of the sensitivity studies for the turbulence buoyancy model (SGDH, GGDH) show that there was not much effect to the pressure, velocity and temperature, because the main phenomenon, *i.e.* jet and condensation flows are aligned with the vertical direction and therefore the transverse-stream density gradient had no noticeable impact.

Second, the calculated velocities for the steady-state 2 corresponding to the jet configuration are in good agreement with that of experiments more than that of the steady-state 1 and 4 which correspond to the jet and plume configuration. On the other hand, the calculated temperature distribution was in agreement with the experiments for all steady-states.

Third, the helium volume fraction in the steady-state 4 (with three gases) is higher in the upper region of the vessel, whereas the steam volume fraction becomes higher in the lower vessel region. The calculated helium and steam volume fractions are in good agreement with experimental results.

The simulations confirmed the formation of two large circulation streams. In the upper region of the vessel (above the injection elevation) the circulation stream is driven by the jet-plume and the condensation flow, whereas in the lower region of the vessel (below the injection elevation) the circulation stream is driven by the natural convection. Moreover, there are also other flow patterns, identified as stagnant, residual and resulting flows. The mixing zone was observed in the middle of the vessel where is located the boundary region between the two large circulation streams.

We have computed virtual cases with the non-condensing wall temperature set at 108 °C and 140 °C. These temperatures are consistent with containment temperature under postulated accident scenario. The virtual case with 140 °C wall temperature shows that the buoyant flow induced by the large temperature differences between the non-condensing wall and the ambient create the two large circulation streams. These two circulation streams remain for the entire simulation. While the virtual case of 108 °C indicates that it is hard to identify those two large circulation streams due to the very low momentum in both regions.

Declaration of competing interest

The authors declare that they have no known competing financial interests or personal relationships that could have appeared to influence the work reported in this paper.

Acknowledgments

We would like to thank to Dr. Emmanuel Porcheron (IRSN, France) for providing the ISP-47 TOSQAN experimental data and test reports.

References

[1] H. Dimmelmeier, J. Eyink, M.A. Movahed, Computational validation of the EPR™ combustible gas control system, Nucl. Eng. Des. 249 (2012) 118–124.
[2] B.R. Sehgal, Nuclear Safety in Light Water Reactors, first ed., Academic Press, 2012.
[3] F. Dabbene, J. Brinster, D. Abdo, E. Porcheron, P. Lemaitre, G. Mignot, R. Kapulla, S. Paranjape, M. Kamnev, A. Khizbullin, Experimental activities on stratification and mixing of a gas mixture under the conditions of a severe accident with intervention of mitigating measures performed in the ERCOSAM-SAMARA projects, in: International Congress on Advances in Nuclear Power Plants, Nice, France, May 3-6, 2015.
[4] E. Studer, J.P. Magnaud, F. Dabbene, I. Tkatschenko, International standard problem on containment thermal–hydraulics ISP47: step 1-Results from the MISTRA exercise, Nucl. Eng. Des. 237 (2007) 536–551.
[5] C. Kaltenbach, E. Laurien, CFD simulation of spray cooling in the model containment Thai, Nucl. Eng. Des. 328 (2018) 359–371.
[6] B.U. Bae, J.B. Lee, Y.S. Park, J. Kim, K.H. Kang, Integral effect test for steam line break with coupling reactor coolant system and containment using ATLAS-CUBE facility, Nucl. Eng. 53 (2021) 2477–2487.
[7] M. Ishigaki, S. Abe, Y. Sibamoto, T. Yonomoto, Experimental investigation of density stratification behavior during outer surface cooling of a containment vessel with the CIGMA facility, Nucl. Eng. Des. 367 (2020), 110790.
[8] D. Paladino, et al., Outcomes from the EURATOM-ROSATOM ERCOSAM SAMARA projects on containment thermal-hydraulics for severe accident management, Nucl. Eng. Des. 308 (2016) 103–114.
[9] D. Paladino, R. Kapulla, S. Paranjape, S. Suter, C. Hug, M.S. Chae, M. Andreani, PANDA experimental database and further needs for containment analyses, Nucl. Eng. Des. 404 (2023), 112173.
[10] CSNI International Standard Problems, ISP, Brief Descriptions, 1975-1999.
[11] J. Malet, E. Porcheron, J. Vendel, OECD International Standard Problem ISP-47 on containment thermal-hydraulics-Conclusions of the TOSQAN part, Nucl. Eng. Des. 240 (2010) 3209–3220.
[12] International Csni, Standard Problem ISP-47 on Containment Thermal Hydraulics, Final report, 2007.
[13] S. Kelm, H. Müller, H.J. Allelein, A Review of the CFD modeling progress triggered by ISP-47 containment thermal hydraulics, Nucl. Sci. Eng. 193 (2019) 63–80.
[14] J. Vendel, P. Cornet, J. Malet, E. Porcheron, H. Paillère, M.L. Caron-Charles, E. Studer, K. Fischer, H.J. Allelein, ISP 47 'Containment thermal hydraulics' Computer codes exercise based on TOSQAN, MISTRA and Thai experiments, in: EUROSAFE Congress, Berlin, Germany, 2002.
[15] S. Kelm, M. Kampili, X. Liu, A. George, D. Schumacher, C. Druska, S. Struth, A. Kuhr, L. Ramacher, H.J. Allelein, K.A. Prakash, G.V. Kumar, The tailored CFD package 'containmentFOAM' for analysis of containment atmosphere mixing, H2/CO Mitigation and Aerosol Transport, Fluids 6 (2021) 1–21.
[16] M. Kampili, G. Vijaya Kumar, S. Kelm, K. Arul Prakash, H.J. Allelein, CFD simulations of stratified layer erosion in MiniPanda facility using the tailored CFD solver containmentFOAM, Int. J. Heat Mass Tran. 178 (2021), 121568.
[17] N.C. Markatos, M.R. Malin, G. Cox, Mathematical modeling of buoyancy-induced smoke flow in enclosures, Int. J. Heat Mass Tran. 25 (1982) 63–75.
[18] B.J. Daly, F.H. Harlow, Transport equations in turbulence, Phys. Fluids 13 (1970) 2634–2649.
[19] C.R. Wilke, A viscosity equation for gas mixtures, J. Chem. Phys. 18 (1950) 517–519.
[20] G.V. Kumar, L.M.F. Cammiade, S. Kelm, K.A. Prakash, W. Rohlfs, Implementation of a CFD model for wall condensation in the presence of non-condensable gas mixtures, Appl. Therm. Eng. 187 (2021), 116546.
[21] B.A. Kader, Temperature and concentration profiles in fully turbulent boundary layers, Int. J. Heat Mass Tran. 24 (1981) 1541–1544.
[22] E.N. Fuller, K. Ensley, J.C. Giddings, Diffusion of halogenated hydrocarbons in helium. The effect of structure on collision cross sections, J. Phys. Chem. 73 (1969) 3679–3685.
[23] ANSYS Meshing User's Guide, Release 13.0, November 2010, pp. 101–117.
[24] J. Malet, E. Porcheron, J. Vendel, Filmwise condensation applied to containment studies: conclusions of the TOSQAN air-steam condensation tests, in: International Topical Meeting on Nuclear Reactor Thermal-Hydraulics (NURETH-11), Avignon, France, October 2-6, 2005.
[25] M. Andreani, D. Paladino, T. George, Simulation of basic gas mixing tests with condensation in the PANDA facility using the Gothic code, Nucl. Eng. Des. 240 (2010) 1528–1547.
[26] D. Paladino, R. Zboray, P. Benz, M. Andreani, Three-gas mixture plume inducing mixing and stratification in a multi-compartment containment, Nucl. Eng. Des. 240 (2010) 210–220.